

Magnetotransport of fluxoids in intermediate-phase type-II superconducting NbN thin films around T_c

Sai Vaishnavi Kanduri ^{1,2,*}, Sahitya V. Vegesna ^{1,2,†}, Danilo Bürger,³ Zichao Li,⁴
Detlef Born,¹ and Heidemarie Schmidt ^{1,2,‡}

¹Leibniz Institute of Photonic Technology, 07745 Jena, Germany

²Institute for Solid State Physics, Friedrich Schiller University Jena, 07743 Jena, Germany

³Helmholtz-Zentrum Dresden-Rossendorf (HZDR) Innovation GmbH, Bautzner Landstraße 400, 01328 Dresden, Germany

⁴Institute of Ion-Beam Physics and Materials Research, Helmholtz-Zentrum Dresden-Rossendorf (HZDR),
Bautzner Landstraße 400, 01328 Dresden, Germany



(Received 28 July 2023; revised 31 March 2024; accepted 30 April 2024; published 8 July 2024)

The mixed state transport properties of type-II superconductors are strongly influenced by the dynamic behavior of quantized magnetic fluxoids around the critical temperature (T_c), where a combination of normal and superconducting properties is exhibited. To understand the mixed state transport properties of type-II superconducting NbN ultrathin films (2D) we measured sheet resistance (R_{xx}^M) and Hall resistance (R_{xy}^M) of a 5-nm-thick NbN film around T_c (10.75 K) at temperatures 10.40, 10.68, and 10.77 K. Hall resistance (HR) was measured in external out-of-plane and in-plane magnetic fields up to 6 T, using 100 μ A and 1 mA driving current in Van der Pauw geometry. The electric field of applied bias and Lorentz force of applied external magnetic field causes a movement of the normal conducting electrons within each fluxoid. The moving fluxoids cause dissipation and generation of Hall voltage. We developed a macroscopic analysis of the Hall resistance arising from fluxoids, to advance the differentiation between dissipating current and superconducting currents in type-II superconductors at T_c . We have extracted the number of normal conducting carriers per fluxoid and areal density and mobility of the fluxoids in dependence on the external magnetic field. This differentiation provides valuable insights into the dissipation mechanisms observed during transport measurements, e.g., after localized heating due to single photon absorption in nanostructured type-II superconductors. Furthermore, the developed macroscopic analysis of Hall resistance of fluxoids shows promising potential for investigating the fundamental aspects of fluxoid-defect interactions in type-II superconductors.

DOI: [10.1103/PhysRevResearch.6.033032](https://doi.org/10.1103/PhysRevResearch.6.033032)

I. INTRODUCTION

In recent years, due to its exceptional superconducting properties such as high critical temperatures (T_c) of around 16 K [1], high critical current densities (J_c), and low energy gaps within the transition range [2], type-II superconducting niobium nitride (NbN) has emerged as a highly appealing material for a range of applications including particle accelerators, superconducting electronics, and single photon detectors [3–5]. The transition range, commonly referred to as the range where the normal and superconducting properties coexist, is the region between the lower critical field (H_{c1}) and the upper critical field (H_{c2}) of a superconductor. A comprehensive understanding of the conduction phenomenon in type-II superconducting NbN thin films within

the transition range holds paramount importance for both fundamental research and technological applications. To elucidate the underlying mechanism of superconductivity and transport properties of type-II superconducting materials, understanding vortex dynamics and their response to electric and magnetic fields are considered to be crucial [6,7]. The formation of vortices in NbN thin films (Fig. 1) occurs when the strength of external magnetic field ($H_{o/p}$) lies between H_{c1} and H_{c2} . The surface screening currents generated by the Meissner effect exhibit diamagnetic behavior below H_{c1} . At $H_{c1} < H_{o/p} < H_{c2}$, the superconductor is penetrated by the external magnetic field as vortices, each enclosing a quantum of magnetic flux (ϕ_0) as depicted in Fig. 1(a). The supercurrent encircling each vortex is generated by the two electrons forming a Cooper pair, which extends up to a distance determined by the Ginzburg Landau penetration length [see Fig. 1(c)] [8]. The areal density of superconducting carriers remains homogeneous over the whole type-II superconducting film except at the position of vortices. Intriguingly, under the presence of a magnetic field, mobile vortices tend to arrange themselves in a lower energy lattice, i.e., either in square or in hexagonal configuration as illustrated in Fig. 1(b). When an electric field is applied in addition to the magnetic field, the normal conducting electrons within each mobile vortex experience both a Lorentz force (F_L) and an electric field force

*sai.lanka@uni-jena.de

†sahitya.vegesna@uni-jena.de

‡heidemarie.schmidt@uni-jena.de

Published by the American Physical Society under the terms of the Creative Commons Attribution 4.0 International license. Further distribution of this work must maintain attribution to the author(s) and the published article's title, journal citation, and DOI.

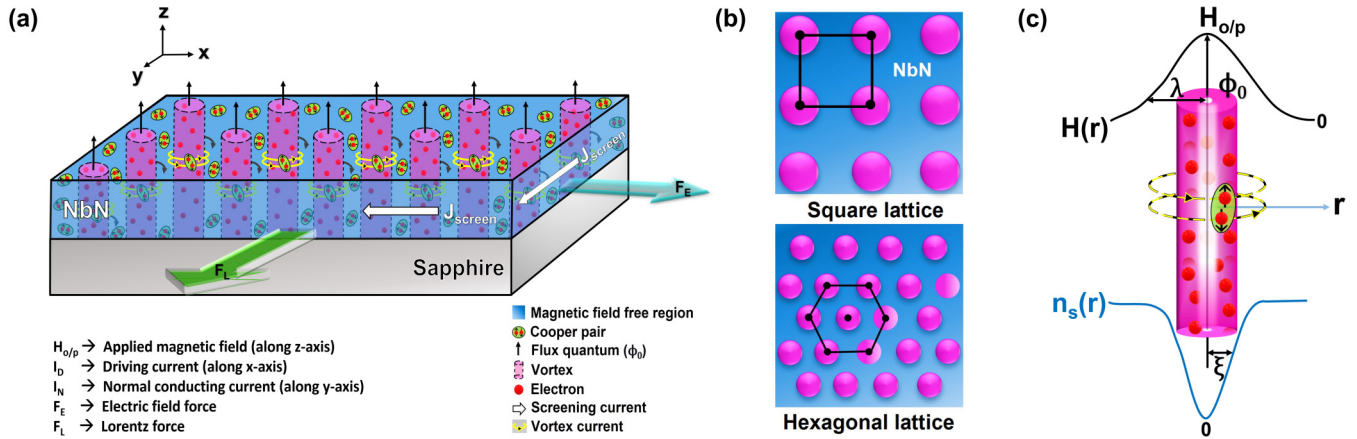


FIG. 1. Schematic representation of Abrikosov vortex lattice in the mixed conducting state of a 5-nm-thick type-II superconducting NbN thin film on 0.5-mm-thick sapphire substrate. Each vortex carries one quantum of magnetic flux (ϕ_0) (a) Lorentz force (F_L) (green arrow) and electric field force (F_E) (blue arrow) acting on normal conducting electrons in each vortex for an out-of-plane applied magnetic field ($H_{c1} < H_{o/p} < H_{c2}$). (b) (Top) Square lattice and (Bottom) hexagonal Abrikosov vortex lattice. The type of lattice depends on an area-optimized equilibrium configuration. (c) Single Abrikosov vortex circled by superconducting current (J_S) which is caused by the two electrons forming the Cooper pair. Radial dependence of out-of-plane magnetic field $H_{o/p}(r)$ and superconducting electron pair (Cooper pair) density $n_s(r)$. The magnetic field is largest at the center ($r = 0$) of the vortex and decreases with an exponential factor of the Ginzburg Landau penetration length (λ). Cooper pair density $n_s(r)$ is smallest at the center of the vortex and increases with an exponential factor of coherence length (ξ).

(F_E), respectively. Mobile vortices causing dissipation when moving are referred to as fluxoids. As a consequence, the normal conducting electrons in the vortices are transported through a milieu of Cooper pairs, causing dissipation, and subsequently initiating the motion of vortices, thereby yielding a Hall resistance [9] of fluxoids. In type-II superconductors, the presence of defects and impurities introduces irregularities in the crystal field potential, which in turn affects the arrangement of vortices. Some of these vortices become permanently localized within regions characterized by low crystal field potential. This phenomenon known as vortex pinning [10], results in an irregular distribution of these pinned vortices throughout the superconducting material. The application of both electric and magnetic fields during magnetotransport experiments can induce changes in the crystal field of the type-II superconducting material. This alteration in the crystal field can lead to a transition between the pinned and mobile flux lines. While the presence of pinned flux lines typically has negligible impact on magnetotransport properties, their transformation into mobile flux lines can profoundly influence the magnetotransport characteristics of the material.

Examining the dynamic behavior of the fluxoids in the presence of an external electric and magnetic field sheds light on the macroscopic properties of fluxoids in type-II superconductors around T_c . In our previous work [11], we performed measurements and analysis of the magnetotransport properties of type-II superconducting NbN ultrathin films (2D) in the normal conducting regime (above T_c) and then extracted temperature dependent Coulomb interaction constants, spin-orbit scattering lengths, localization lengths, and valley degeneracy factors revealing ordinary conduction. The main focus of this paper is to distinguish between superconducting current and dissipating current using a macroscopic approach. The developed macroscopic approach not only enables the distinction between two types of current flowing through the NbN but also provides a pathway for future investigations

into the understanding of fluxoid-defect interactions in type-II superconductors.

II. METHODOLOGY

From our previous work [11], we chose the polycrystalline NbN thin film with a thickness of 5 nm. This film was fabricated on a 0.5-mm-thick insulating sapphire substrate with a nominal size of $1 \times 1 \text{ cm}^2$ using plasma enhanced atomic layer deposition (PEALD). During this process, the substrate temperature was maintained at 380°C , with (tert-butylimido)-tris (diethylamido)-niobium (TBTDEN) and hydrogen plasma serving as precursors. Extensive details concerning the characteristics of NbN films and the PEALD deposition process can be found in references [12–14]. The critical temperature (T_c) of the 5-nm-thick NbN thin film was determined to be 10.75 K [11], which is lower than the T_c of bulk NbN (16.2 K) [15]. Hall resistance (R_{xy}^M) and sheet resistance (R_{xx}^M) of the synthesized NbN thin films (2D) were measured using Van der Pauw geometry around T_c at temperatures of 10.40, 10.68, and 10.77 K. These measurements were performed using the Lake Shore HMS 9700A Hall measurement system in external out-of-plane and in-plane magnetic fields of up to 6 T, with a driving current (I_D) of 100 μA and 1 mA. We developed a macroscopic approach to analyze the measured data and extracted macroscopic parameters of fluxoids, namely the number of normal conducting carriers per fluxoid, areal density, and mobility of the fluxoids in dependence on external magnetic field. The underlying core idea of our macroscopic analysis approach was to establish the link between normal conducting resistivity, measured resistivity, and the superconducting current. A comprehensive illustration of the entire process, from sample preparation to data analysis, is presented in Fig. 10 (Appendix), offering a visual representation that outlines the various steps involved.

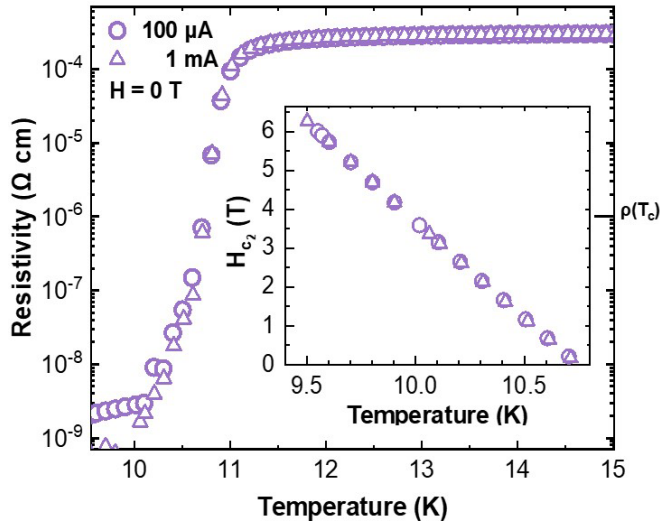


FIG. 2. Temperature dependent resistivity (ρ_{xx}^M) of a 5-nm-thick NbN thin film on sapphire in Van der Pauw geometry at zero field for an applied current of 100 μA and 1 mA. The critical temperature was defined at $\rho(T_c) \approx 1 \mu\Omega \text{ cm}$ for generalization. The inset figure shows the temperature dependence of upper critical magnetic field (H_{c2}) in a temperature range from 9.50 to 10.80 K.

III. ANALYSIS AND DISCUSSION OF RESULTS

Figure 2 shows the temperature dependent resistivity of a 5-nm-thick NbN thin film within the temperature range of 9–15 K under the absence of an external magnetic field. In this work, we defined the critical temperature as the temperature where the resistivity dropped to 1 $\mu\Omega \text{ cm}$, which we determined to be 10.75 K. By utilizing the widely accepted generalized Ginzburg-Landau (G-L) model [16], we estimated the upper critical field (H_{c2}) over a temperature range spanning from 9.50 to 10.80 K (refer to the inset of Fig. 2). The G-L model describes the temperature dependence of the upper critical magnetic field as follows:

$$H_{c2}(T) = H_{c2}(0) \left(\frac{(1-t^2)}{(1+t^2)} \right). \quad (1)$$

where, $H_{c2}(0) = \phi_0/2\pi\xi(0)^2$ is the upper critical field at 0 K, ϕ_0 is the magnetic flux quantum, $t = T/T_c$ is the reduced temperature and $\xi(0)$ is the Ginzburg-Landau coherence length. The coherence length of 5-nm-thick NbN thin film, based on literature values [17,18], is considered to be 2.54 nm. Our observations revealed a gradual reduction in H_{c2} from 6 T at 9.6 K to 0 T at 10.75 K, ultimately determining the critical temperature to be approximately 10.75 K (inset in Fig. 2).

The transport properties of NbN thin films in Van der Pauw geometry were analyzed from magnetic field dependent sheet resistance measurements for both out-of-plane and in-plane configurations around T_c . The NbN thin film resistivity (ρ_{xx}^M) in Fig. 3 is related to sheet resistance as ($R_{\text{sheet}} \times \text{thickness}$). The observed increase in resistivity with the magnetic field can be attributed to the increase in the number of moving vortices (fluxoids) [19], resulting in dissipation and an accompanying rise in normal conducting current due to the breaking of Cooper pairs. At higher fields, the resistivity $\rho_N(T)$ was approximately around 270 $\mu\Omega \text{ cm}$ which is comparable to

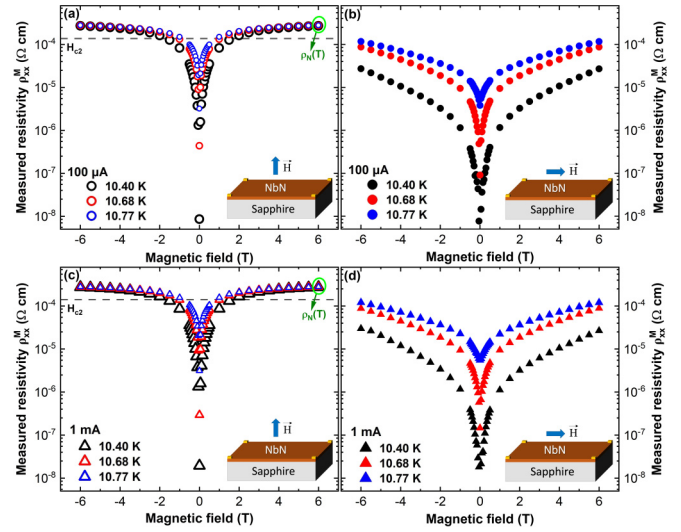


FIG. 3. Resistivity (ρ_{xx}^M) obtained from measured sheet resistance in Van der Pauw geometry as a function of magnetic field in out-of-plane (o/p, open symbols) and in-plane (i/p, closed symbols) configuration at three temperatures (10.40, 10.68, and 10.77 K) around T_c on a 5-nm-thick NbN thin film on sapphire in the magnetic field range from -6 to $+6$ T with a driving current of [(a) and (b)] 100 μA and [(c) and (d)] 1 mA. At higher fields, measured resistivity (ρ_{xx}^M) (marked in green) reaches the resistivity of normal conducting NbN $\approx 270 \mu\Omega \text{ cm}$.

the resistivity obtained at normal conducting temperatures recorded in Ref. [11]. The anisotropic behavior in resistivity between in-plane and out-of-plane configurations with magnetic field can be ascribed to the contribution of fluxoids to mixed-state conductivity.

A. Hall resistance of fluxoids

The magnetotransport measurements were conducted in two different regimes. In regime 1 (mixed), both superconducting and dissipating currents coexist. For these measurements, the temperature was maintained just below the critical temperature ($T_c \lesssim T_c$), while the magnetic field was varied above H_{c1} ($\approx 10^{-4}$ T) and below H_{c2} (≈ 1.5 T) (see Fig. 4). In regime 2 (normal), dissipating currents predominate. Here,

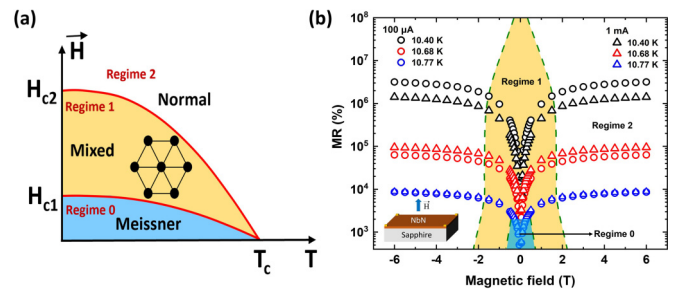


FIG. 4. (a) Phase diagram of type-II superconductor showing three different regimes. (b) Measured magnetoresistance in out-of-plane magnetic field at the driving current set at 100 μA (circles) and 1 mA (triangles) at 10.40, 10.68, and 10.77 K for 5nm-thick NbN film on sapphire.

the temperature was set a few Kelvin above the critical temperature $T_c(\geq T_c)$, with magnetic field ranging from 0 to 6 T. To distinguish between dissipating and superconducting current, an initial analysis was performed on the magnetoresistance obtained from magnetotransport measurements conducted within both regimes. Magnetoresistance (MR%) is defined as the change in longitudinal resistivity (sheet resistivity) at a nonzero magnetic field $\rho(H, T)$ minus the longitudinal resistivity at zero magnetic field $\rho(0, T)$, divided by the longitudinal resistivity at zero magnetic field $\rho(0, T)$ multiplied with 100%.

$$MR = \frac{\rho(H, T) - \rho(0, T)}{\rho(0, T)} \times 100\%. \quad (2)$$

In regime 1, the magnetoresistance exceeded at least +100% and reached values way more than 10 000%. The smallest MR in regime 1 (MR = +100%) just above T_c where H_{c2} is close to zero is depicted in Fig. 4(b). In regime 2, the magnetoresistance remained below +10% [11] when compared to MR values obtained just below T_c . Following our analysis of MR in regime 1, we assumed that the normal conducting carriers are purely dependent on temperature and have a negligible field dependence.

$$\rho_{xx}^N(H, T) = \rho_N(T), \quad (3)$$

where $\rho_{xx}^N(H, T)$ is the normal conducting resistivity. Next, we analyzed magnetotransport measurement in regime 1 where we measured resistivity [$\rho_{xx}^M(H)$] under a constant driving current (I_D) of 100 μ A and 1 mA. The measured resistivity encapsulates contributions from both superconducting and normal conducting carriers.

$$\rho_{xx}^M(H, T) = \frac{V_M}{I_D} \times t, \quad (4)$$

where V_M is the measured longitudinal voltage, I_D is the driving current, and t is the film thickness. The measured longitudinal voltage is subdivided over two current paths: one for the superconducting current I_S and another for the dissipating/normal conducting current I_N . In general, the total driving current is expressed as follows:

$$I_D = I_S(H) + I_N(H), \quad (5)$$

where I_S and I_N are currents from superconducting and normal conducting carriers. Note that the subscripts D, S, N, and M symbolize driving, superconducting, normal conducting, and measured, respectively. Taking into account the absence of contribution from the superconducting current to the normal resistivity, we formulated the interrelation between normal conducting resistivity (ρ_{xx}^N), measured resistivity (ρ_{xx}^M), superconducting current (I_S), and driving current (I_D) as

$$\rho_{xx}^N(H, T) = \frac{V_M}{(I_D - I_S)} \times t, \quad (6)$$

where V_M is the measured longitudinal voltage, $I_D - I_S$ is the normal conducting current, and t is the film thickness. Reiterating Eqs. (4)–(6), we get

$$\rho_{xx}^N(H, T) = \rho_{xx}^M(H, T) \left(\frac{I_D}{I_D - I_S(H)} \right). \quad (7)$$

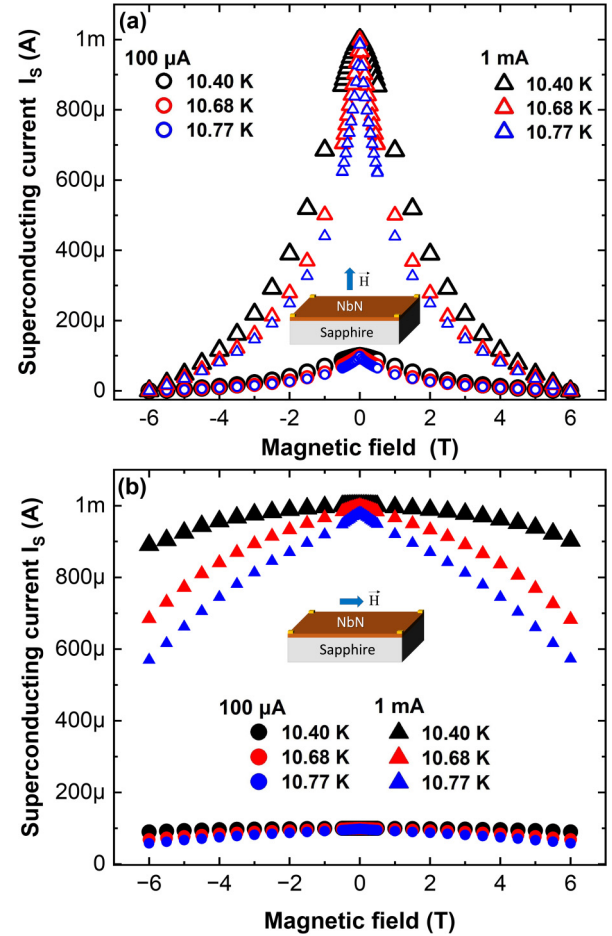


FIG. 5. Superconducting current (I_S) derived from the measured resistivity (ρ_{xx}^M) using Eq. (8) as a function of (a) out-of-plane (o/p, open symbols) and (b) in-plane (i/p, closed symbols) magnetic field at 10.40, 10.68, and 10.77 K for a 5-nm-thick NbN film on sapphire in the magnetic field range from -6 to $+6$ T with an applied current of 100 μ A and 1 mA. With an increase in temperature, the superconducting current (I_S) decreases.

By considering the approximation from Eq. (3) in the mixed conduction of regime 1, we analyzed $I_S(H)$ (see Fig. 5) using following expression:

$$I_S(H) = I_D \left(1 - \frac{\rho_{xx}^M(H)}{\rho_N(T)} \right). \quad (8)$$

At a zero field, the maximum superconducting current equates to the driving current, which signifies that the whole sample is superconducting. For a fixed temperature, I_S decreases with the applied magnetic field and tends to zero [see Fig. 5(a)] due to the presence of dissipative vortices. As anticipated, fluxoid formation is not discernible from in-plane magnetic field measurements due to the film's length (1 cm) and the magnetic field's inability to permeate the entire sample. Consequently, the superconducting current carried by the Cooper pairs does not completely approach zero with an increase in magnetic field [see Fig. 5(b)].

The transport properties of fluxoids in NbN thin films in mixed normal and superconducting state around T_c region were analyzed from Hall effect measurements for both

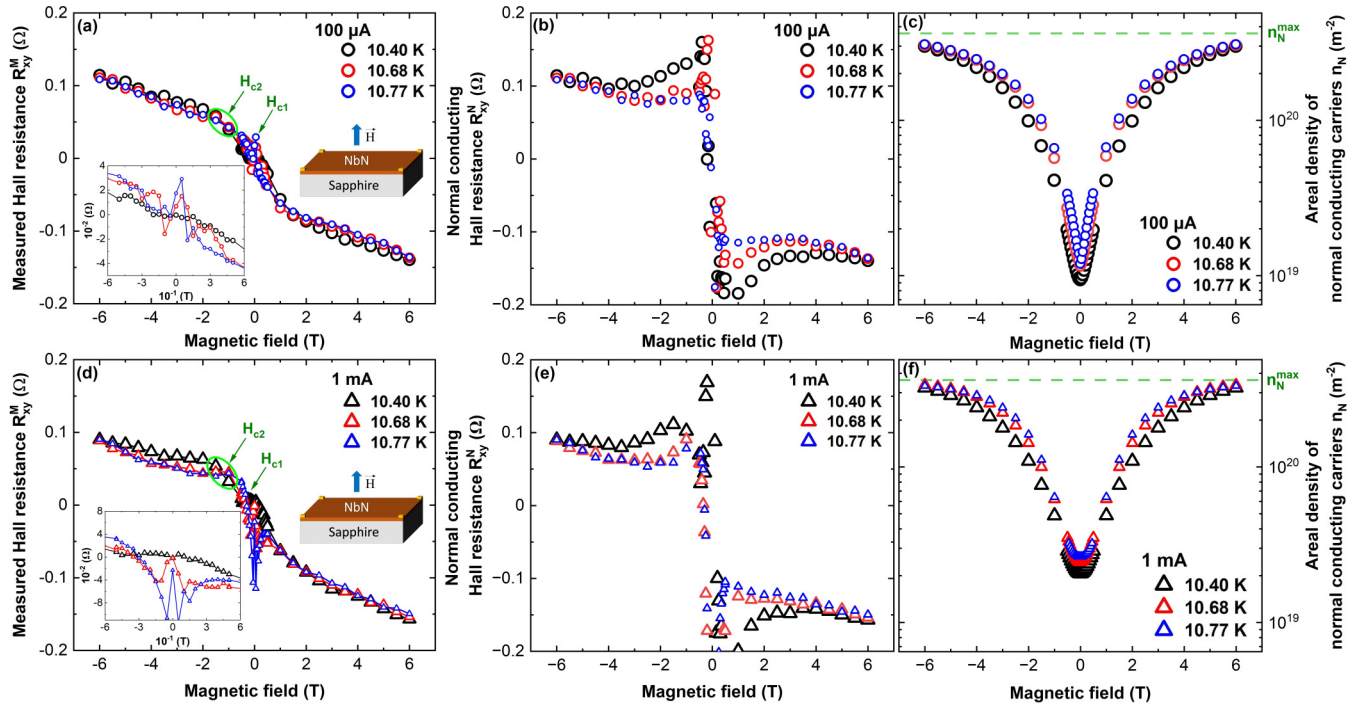


FIG. 6. [(a) and (d)] Hall resistance (HR) measured in Van der Pauw geometry at 10.40, 10.68, and 10.77 K for a 5-nm-thick NbN film on sapphire. The inset figures shows a magnified view around ± 0.6 T where the noise is reduced when approaching $T = 10.40$ K. Mixed state conduction window has been recognized between critical fields around $H_{c1} = \pm 0.1$ T and $H_{c2} = \pm 1.5$ T (highlighted in green) where a nonlinear behavior of magnetic field dependent Hall resistance is observed. Negative slope of Hall resistance indicates n -type carrier conduction. [(b) and (e)] Derived normal conducting Hall resistance (R_{xy}^N) [using Eq. (9)] as a function of magnetic field. [(c)–(f)] Derived areal density of normal conducting carriers (n_N) [using Eqs. (11) and (A3)] showing the number of normal conducting carriers per fluxoid per unit area of fluxoid lattice as a function of magnetic field. The applied current was [(a)–(c)] 100 μ A and [(d)–(f)] 1 mA.

out-of-plane and in-plane configurations. The change in Hall resistance (HR) with the magnetic field at temperatures 10.40, 10.68, and 10.77 K is shown in Figs. 6(a) and 6(d). Due to the presence of normal conducting carriers confined within each fluxoid in the mixed state region of chosen type-II NbN superconducting thin film, we observe a change in Hall resistance (HR) with a magnetic field. Previous investigation [11] on NbN above T_c revealed a negative linear dependence of Hall resistance at normal conducting temperatures. The nonlinear response exhibited by the Hall resistance at low magnetic fields around T_c indicates a significant variation in carrier concentration [20,21]. Based on the raw data, we observe a direct proportionality between temperature and noise which is evident in both cases ($I = 100 \mu$ A and 1 mA) at around ± 0.6 T. This can be substantiated from inset figures in Figs. 6(a) and 6(d) where the data at 10.40 K resemble our theoretical expectations with minimum deviations. In regime 1, the measured Hall resistance [$R_{xy}^M(H)$] comprises both the superconducting and normal conducting carriers. By utilizing measured Hall resistance $R_{xy}^M(H)$, we describe the Hall resistance from the ordinary conduction $R_{xy}^N(H)$ [see Figs. 6(b) and 6(e)], which is specifically attributable to normal conducting fluxoids as follows:

$$R_{xy}^N(H) = \frac{R_{xy}^M(H)}{\left(1 - \frac{I_s(H)}{I_D}\right)}. \quad (9)$$

From the classical Hall resistance, the carrier concentration is expressed as [22]

$$n = \frac{-H}{R_{xy} \times (\text{charge}) \times (\text{thickness})}. \quad (10)$$

We considered ($n \times t$) as the areal density of normal conducting carriers $n_N(H)$, which is defined as the number of normal conducting electrons per fluxoid divided by the unit area of the fluxoid lattice [region covering black line in Fig. 1(b)]. Ideal Hall resistance is zero at zero magnetic field. However, geometrical errors, misalignment of the magnetic field and current directions, sample in-homogeneity, temperature gradients, piezoresistive effects, etc. [23] may cause a nonzero offset of the Hall resistance at zero magnetic field. We corrected this offset and calculated the areal density of normal conducting carriers [$n_N(H)$] throughout the NbN sample using the following equation:

$$n_N(H) = \frac{-H}{R_{xy}^N(H) \times e}, \quad (11)$$

where e is the charge of an electron. Areal density of normal conducting carriers [Figs. 6(c) and 6(f)] has been extracted and fitted from Hall resistance data [Eq. (A3)] after performing an offset correction which is elucidated in detail in Appendix. With an increasing magnetic field the number of vortices increases and the normal conducting regions where electrons move without zero resistance expand. As a consequence, we observe an increase in the areal density of normal

conducting carriers (n_N) across the sample. In regime 2, areal density of normal conducting carriers $n_N(H, T)$ weakly depends on magnetic field and temperature. Therefore $n_N(H, T)$ can be approximated by n_N^{\max} . Areal density of normal conducting carriers n_N is homogenous over the whole type-II superconducting film in this regime. At larger fields, the areal density of normal conducting carriers approaches the maximum value (n_N^{\max}) of bulk NbN at normal conducting temperatures which is approximately $0.362 \times 10^{21} \text{ m}^{-2}$ [11].

B. Macroscopic fluxoid parameters

We examined the transport properties of NbN thin films with a focus on fluxoid motion in the presence of a magnetic field. We extended the classical Hall resistance approach and also included the Hall resistance of fluxoids. In order to maintain a constant magnetic flux ϕ_0 through a single fluxoid, the area of the fluxoid needs to decrease with an increase in magnetic field

$$\phi = HA = \Phi_0. \quad (12)$$

The areal density of fluxoids, defined as the number of fluxoids per unit area [24]

$$n_v = \frac{|H|}{\phi_0}, \quad (13)$$

typically increases with magnetic field and remains constant with temperature. From Eq. (11), considering $n_N \approx n \times t$, the number of normal conducting carriers per fluxoid was calculated by

$$e_v = \frac{n_N(H)}{n_v(H)}. \quad (14)$$

The normal conducting carrier concentration $n_c(T)$ of each flux quantum volume is independent of the external magnetic field and is equivalent to carrier concentration at normal conducting temperatures. By assuming that the shape of fluxoid resembles a perfect cylinder for a macroscopic approach, we derived the radius of the fluxoid (r_v) from $e_v \approx \pi r_v^2 t \times n_c(T)$ as follows:

$$r_v = \left(\frac{1}{\sqrt{\pi \times t \times n_c(T)}} \right) \times \sqrt{e_v}. \quad (15)$$

Figure 7 shows the number of normal conducting carriers per fluxoid (e_v) for temperatures around T_c with a driving current of $I = 100 \mu\text{A}$ and 1 mA . At a specific temperature, with a rise in the magnetic field, we generally expect to see a decrease in e_v because the stronger magnetic field leads to larger vortex density within the sample causing them to occupy less space and to have a small radius. The analysis revealed a notable variation in e_v at around $\pm 1.5 \text{ T}$, exhibiting a decreasing and then increasing trend with magnetic field. This variation can be attributed to the assumption that we considered the fluxoid as a perfect cylinder and also due to changes in size and shape of vortex core within the superconductor which are influenced by the penetration of magnetic field from different dielectric media. We also noticed a direct proportionality of e_v with temperature, particularly at the upper critical field $H_{c2} = \pm 1.5 \text{ T}$. Literature data [25] suggest that one possible reason for the increase in e_v and fluxoid radius (r_v) in type-II

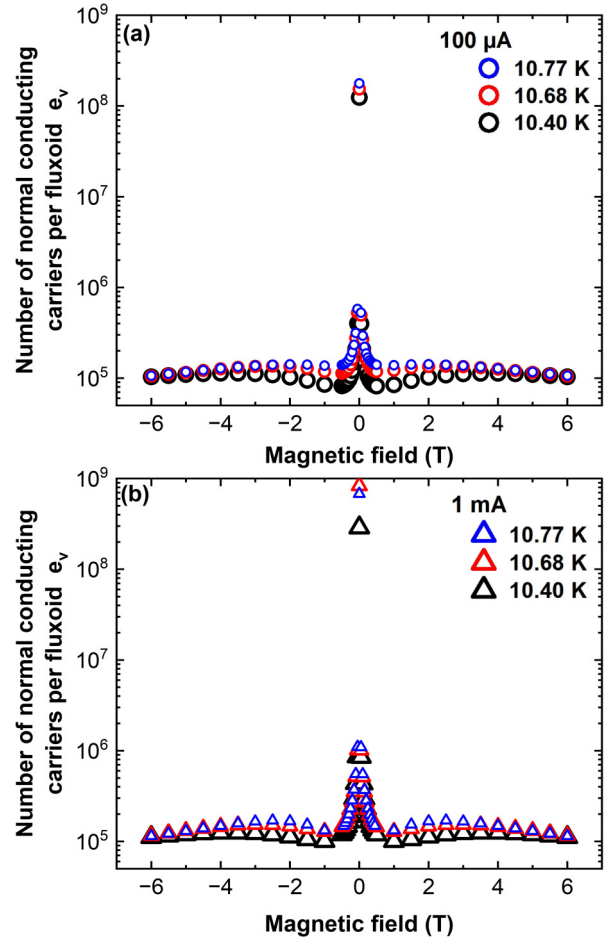


FIG. 7. Number of conducting carriers per fluxoid (e_v) as a function of magnetic field at 10.40, 10.68, and 10.77 K for 5-nm-thick NbN film on sapphire for an applied current of (a) $100 \mu\text{A}$ and (b) 1 mA . The number of conducting carriers per fluxoid increases with measurement temperature approaching T_c .

superconductors with temperature is due to the increase in penetration depth. By considering the sheet resistivity which is related to conductivity as $\sigma = \frac{1}{\rho} = ne\mu$, where n is the carrier concentration, e is the charge, and μ is the mobility, we proceeded to evaluate the mobility of the fluxoids, presuming that normal conducting carriers are purely dependent on temperature and have a negligible field dependence. Using the relation between resistivity and conductivity we determine $\sigma_N(T)$. The calculation of mobility was carried out using the following relation:

$$\mu_v = \frac{\sigma_N(T) \times t}{n_v \times (e_v \times e)}. \quad (16)$$

where n_v is the areal density of fluxoids [in Eq. (13)], t is the film thickness, $(e_v \times e)$ is the total charge of one fluxoid defined as the number of normal conducting carriers per fluxoid (e_v) multiplied with electron charge. We observe an inversely proportional behavior of mobility of fluxoids with magnetic field around T_c (see Fig. 8). At around upper critical field $H_{c2} = \pm 1.5 \text{ T}$ when approaching critical temperature we observe an increase in mobility. The mobility at higher

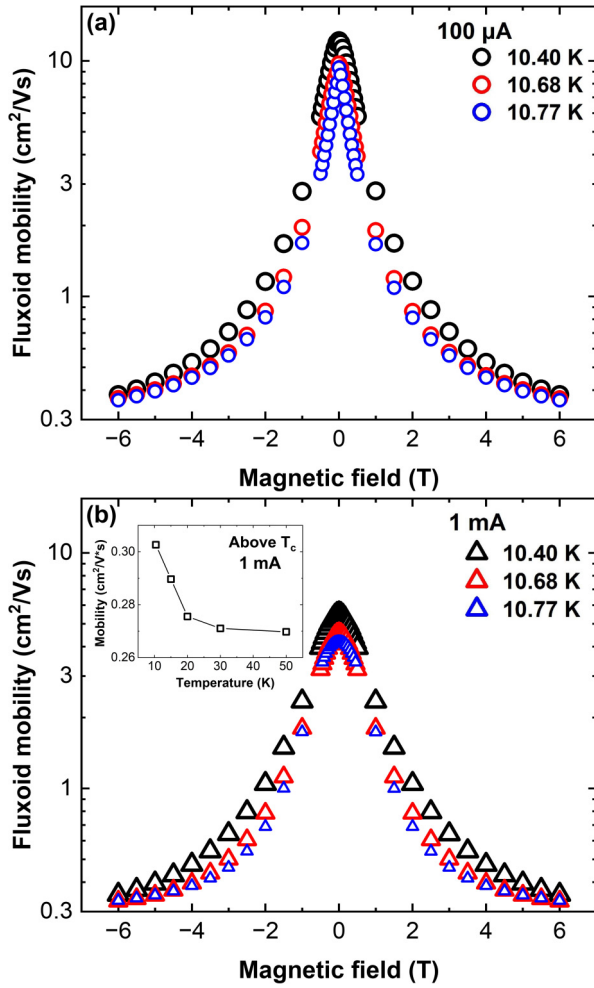


FIG. 8. Fluxoid mobility derived using Eq. (16) and its dependence on magnetic field at 10.40, 10.68, and 10.77 K for a 5-nm-thick NbN film on sapphire with a driving current (a) 100 μA and (b) 1 mA. (b) Inset figure shows the mobility of NbN thin film at normal conducting temperatures [11] for a driving current of 1 mA.

fields is in the range of $0.35 \text{ cm}^2 \text{ V}^{-1} \text{ s}^{-1}$ around T_c . From earlier work [11] at above T_c the carrier mobility was around $(0.26\text{--}0.28) \text{ cm}^2 \text{ V}^{-1} \text{ s}^{-1}$. Extrapolating to temperatures below 15 K, the mobility at 10.40 K is determined to be $0.30 \text{ cm}^2 \text{ V}^{-1} \text{ s}^{-1}$ [refer inset of Fig. 8(b)]. The expected value well agrees with the normal conducting behavior above H_{c2} . This observation accentuates the resemblance between the fluxoid mobility at higher fields ($H_{c2} = \pm 1.5 \text{ T}$) around T_c and the mobility computed above T_c . As the temperature increases, the two electrons within each Cooper pair separate. Thermal fluctuations of these electrons within each fluxoid dictate the properties of fluxoid motions.

IV. CONCLUSION AND OUTLOOK

Using the Hall effect measurement technique, we conducted an analysis on magnetotransport data of a 5-nm-thick superconducting niobium nitride (NbN) film on a sapphire substrate. The measurements were performed with input currents of 100 μA and 1 mA at around critical temperature

T_c (10.40, 10.68, and 10.77 K) in both out-of-plane and in-plane configurations. The magnetoconductivity analysis results above T_c served as input for undergoing research into the dynamics of fluxoids in the mixed state region around T_c . We adopted a macroscopic approach to determine superconducting current based on sheet resistance measurements. By incorporating the classical Hall resistance approach, we extracted fluxoid parameters such as number of conducting charges per fluxoid, areal density, and mobility of the fluxoids. Our observations revealed an increase in areal density and a decrease in number of normal conducting carriers per fluxoid with increasing magnetic field which is consistent with the previous experimental studies. Furthermore, we observed a similarity of mobility around T_c at magnetic fields between H_{c1} and H_{c2} and of mobility at normal conducting temperatures at zero-valued magnetic fields.

Understanding the interplay between superconductivity and resistivity will assist in enhancing the sensitivity of superconducting resistivity sensors, e.g., of superconducting nanowire single-photon detectors (SNSPD) [26] where local heating after absorption of single photons and subsequent hot spot formation is exploited to detect single photon absorption. Despite considerable technological advancements in enhancing the detection efficiency and overall functionality of SNSPDs mainly in the long wavelength spectral range, a comprehensive understanding of the operational mechanisms underlying those superconducting resistivity sensors still remains elusive. Several theoretical models such as the hotspot model, electrothermal model, diffusion model, and vortex-based model [5,27–30], have been put forward to elucidate the operational principles of SNSPDs, thus providing insights into the behavior of today's most widely used single photon detector in quantum technology. These macroscopic models suggest that the genesis of hot spots is pivotal to the SNSPD's mechanism, which is attributed to vortex motion across biased superconducting nanowires. Nevertheless, to date, no microscopic theoretical model has been developed to account for the generation of a vortex-antivortex pair in the vicinity where a hot spot is formed or for the contributions of the vortex motion to hotspot formation. The unfavorable dark counts in SNSPDs have been linked to the vortex-crossing mechanism [31,32], but strategies to reduce them have not yet been extensively investigated.

Our manuscript elucidates the mixed-state transport properties of type-II superconductors by quantitatively analyzing fluxoid dynamics near the critical temperature (T_c). We provide insights into the microscopic dissipative mechanisms in the mixed state, highlighting how normal conducting electrons within vortices affect magnetotransport properties, crucial for understanding the superconducting-to-normal transition [33]. Additionally, our study offers new perspectives on quantum phase transitions in type-II superconductors, demonstrating the role of localized variations in carrier density and mobility on macroscopic quantum states and connecting these changes to vortex dynamics [34,35]. Furthermore, by analyzing the Hall resistance of fluxoids, we contribute to the understanding of vortex dynamics, exploring fluxoid mobility, and their pinning and depinning mechanisms under varying external magnetic fields, which is vital for applications of superconductors [36]. This work can be used as a foundation for further

analysis in understanding vortex motion in superconducting resistivity sensors, e.g., the resulting hotspot formation in SNSPDs.

ACKNOWLEDGMENTS

We thank Mario Ziegler from Leibniz-Institut für Photonische Technologien e.V. for NbN thin film preparation. This research was supported by a financial grant to Danilo Bürger and Heidemarie Schmidt and they acknowledge support from the Deutsche Forschungsgemeinschaft (Grant Code: BU 2956/1-1 and SCHM 1663/4-1). Sahitya V. Vegesna acknowledges funding from the Federal Ministry of Education and Research, APPA Photon (Code: 074023-02 BMBF), and from the Office of Technology Assessment at the German Bundestag, TAB-AIF QHub (Code: K203178), and from the Carl-Zeiss-Stiftung (CSZ Center QPhoton). Sai Vaishnavi Kanduri acknowledges funding from DFG META Active (Code: GRK 2675). We acknowledge support by the German Research Foundation Project No. 512648189 and the Open Access Publication Fund of the Thuringian University and State Library Jena.

APPENDIX

The areal density of normal conducting carriers (n_N) shown in Figs. 6(c) and 6(f) was obtained after performing offset correction and logistic fitting. A closer look at the Hall resistance plot in Figs. 6(a) and 6(d) reveals noise around zero field, which can be mitigated through smoothing techniques such as the adjacent averaging method, Savitzky-Golay method, etc. We employed the Savitzky-Golay (SG) method for smoothing the curve due to its efficient polynomial regression performance, making it an ideal method for curve smoothing. However, merely applying the smoothing technique was insufficient, and led to finding better approaches to perform a meaningful statistical analysis of the curve. We performed an offset correction for areal density of normal conducting carriers [Eq. (11)] as detailed below:

$$\Delta n_N(|H|) = n_N(-H) - n_N(+H). \quad (\text{A1})$$

Offset correction on n_N has been done separately for positive and negative fields as follows:

$$\begin{aligned} n_N(+H, \text{ after offset correction}) &= n_N(+H) + \frac{1}{2} \Delta n_N, \\ n_N(-H, \text{ after offset correction}) &= n_N(-H) - \frac{1}{2} \Delta n_N. \end{aligned} \quad (\text{A2})$$

TABLE I. Temperature dependent curve parameters of the fitted logistic curve.

Parameters	$I = 100 \mu\text{A}$						$I = 1 \text{ mA}$					
	10.40 K		10.68K		10.77 K		10.40 K		10.68K		10.77 K	
Field	-ve field	+ve field	-ve field	+ve field	-ve field	+ve field	-ve field	+ve field	-ve field	+ve field	-ve field	+ve field
$n_{\max} (\text{m}^{-2})$	3.77×10^{20}	3.54×10^{20}	3.54×10^{20}	3.77×10^{20}	3.77×10^{20}							
$n_{\min} (\text{m}^{-2})$	9.38×10^{18}	9.42×10^{18}	1.22×10^{19}	1.15×10^{19}	1.31×10^{19}	1.19×10^{19}	2.06×10^{19}	2.06×10^{19}	2.44×10^{19}	2.44×10^{19}	2.65×10^{19}	2.65×10^{19}
x_0	13.42	13.31	4.32	5.72	7.28	8.72	11.89	11.89	8.02	8.02	2.12	2.12
h	1.65	1.65	1.68	1.57	1.46	1.41	1.81	1.81	1.90	1.90	2.47	2.47
s	6.66	6.62	1.60	2.26	2.96	3.60	7.42	7.42	6.47	6.47	0.78	0.78

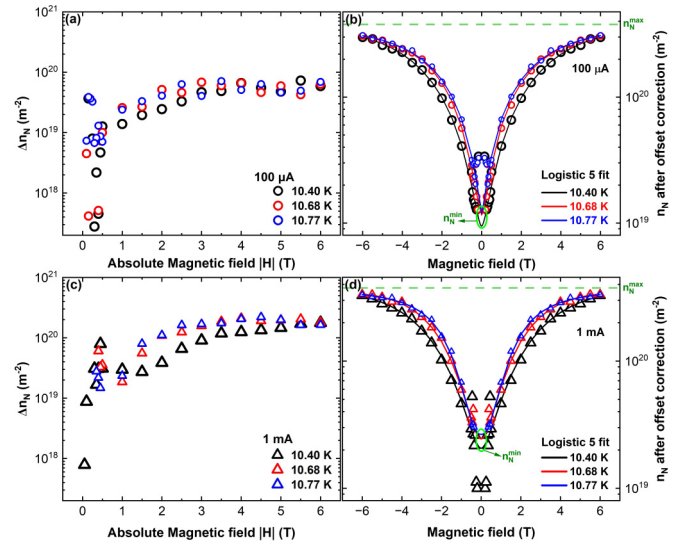


FIG. 9. [(a) and (c)] Offset in areal density of normal conducting carriers is calculated for specific strengths of magnetic field in opposite directions ($+H$ and $-H$) using Eq. (A1). [(b) and (d)] Magnetic field dependent offset correction on normal conducting carrier concentration n_N for positive and negative magnetic fields using Eq. (A2). The solid lines represent the logistic 5 fit [Eq. (A3)] for the offset corrected n_N at 10.40, 10.68, and 10.77 K for 5-nm-thick NbN film on sapphire with an applied current [(a) and (b)] 100 μA and [(c) and (d)] 1 mA. At larger fields, the fitted line of areal density of normal conducting carriers approaches the maximum value n_N (highlighted in green) which is approximately $0.362 \times 10^{21} \text{ m}^{-2}$.

Figures 9(a) and 9(c) illustrates the variation of the offset in areal density of normal conducting carriers with the magnetic field around T_c for an applied current of 100 μA and 1 mA. By considering this offset, an offset correction has been performed on n_N . The offset correction ensured symmetry in the curve. Subsequently, we carried out nonlinear curve-fitting on the offset-corrected normal conducting carrier concentration using a five-parameter logistic regression or logistic 5 model. The logistic 5 equation is given by

$$n_N = n_{\max} + \frac{n_{\min} - n_{\max}}{\left(1 + \left(\frac{\pm x}{x_0}\right)^h\right)^s}, \quad (\text{A3})$$

where n_{\max} and n_{\min} are the lower and upper values of the curve respectively, x is magnetic field (independent variable), x_0 is the inflection point, h is the hill slope, and s is the control

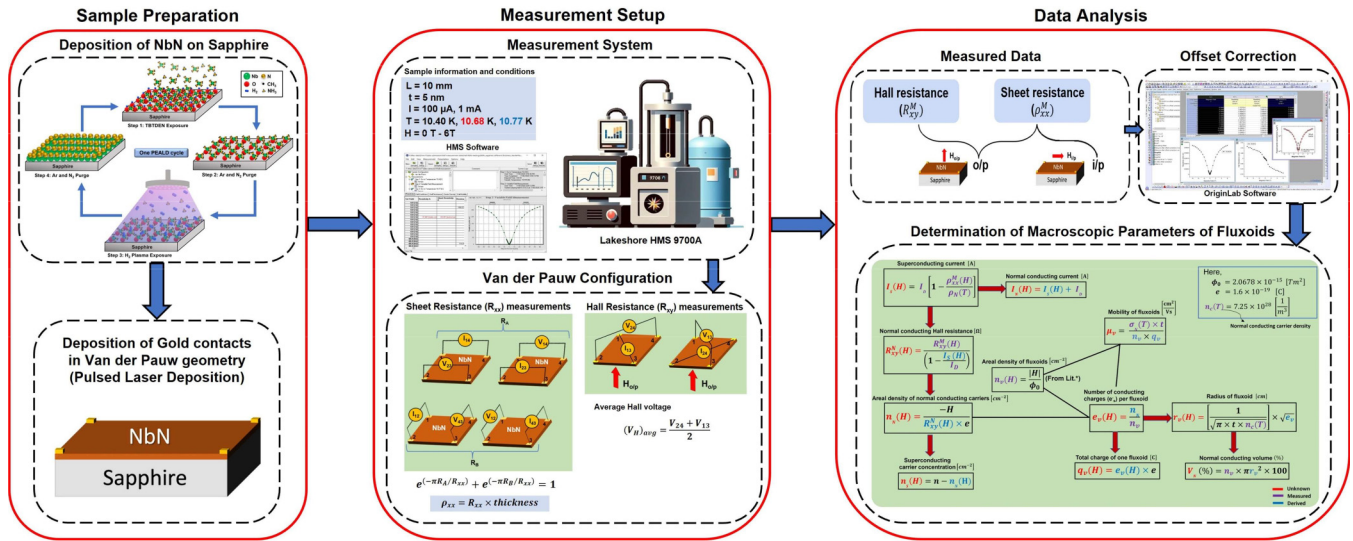


FIG. 10. Flowchart for the analysis of macroscopic parameters of fluxoids in type-II superconducting thin films, namely number of normal conducting carriers per fluxoid, areal density of normal conducting carriers, and mobility of the fluxoids in dependence on the external magnetic field, including sample preparation, measurement and analysis of magnetoresistance.

factor. This function yields statistical values like the residual sum of squares (RSS), coefficient of determination (R^2) which signifies the fitness of the model. A model is said to be a good fit if the RSS value is minimal and R^2 value ranges between 0 and 1 (a general accepted assumption). After investigating different sigmoidal models, the logistic 5 function stood out due to its high R^2 value of 0.996 and a low RSS value, making it most suitable for our analysis. The evaluation of the of the above-mentioned logistic function was performed for two different currents 100 μ A and 1 mA around T_c . The obtained fitted parameters are summarized in Table I. Figures 9(b) and 9(d) demonstrates the variation of areal density of normal conducting carriers after offset correction with the magnetic field and its corresponding logistic 5 fitting around T_c for an applied current of 100 μ A and 1 mA.

The flow chart for the analysis of macroscopic parameters of fluxoids is given in Fig. 10. The figure presents a comprehensive workflow for the preparation, measurement, and analysis of NbN thin films deposited on sapphire substrates. In the sample preparation phase, the NbN films are grown on sapphire via a cyclic process involving trimethylaluminum

(TMA) and NH_3 precursors, with intermediate purging and plasma exposure to ensure high-quality film growth. Following this, gold contacts are patterned on the NbN film using a Van der Pauw geometry through Pulsed Laser Deposition (PLD) for electrical characterization. The measurement setup segment details the experimental parameters and the equipment (Lakeshore HMS 9700A) used for conducting resistance measurements in a Van der Pauw configuration. The setup is calibrated to provide sheet resistance and Hall resistance values at specified magnetic fields and temperatures. The data analysis portion illustrates how the measured resistances are used to correct for any offsets using OriginLab software, followed by the calculation of macroscopic parameters such as the fluxoid’s mobility and superconducting carrier concentration. These parameters are critical for understanding the electronic properties of the NbN films, which could have implications for superconducting applications. The process flows logically from sample preparation through measurement and finally to the analysis of key parameters, emphasizing the thorough and systematic approach taken in the study.

[1] B. T. Matthias, T. H. Geballe, and V. B. Compton, Superconductivity, *Rev. Mod. Phys.* **35**, 1 (1963).
 [2] N. Cucciniello, D. Lee, H. Y. Feng, Z. Yang, H. Zeng, N. Patibandla, M. Zhu, and Q. Jia, Superconducting niobium nitride: A perspective from processing, microstructure, and superconducting property for single photon detectors, *J. Phys.: Condens. Matter* **34**, 374003 (2022).
 [3] S. Leith, M. Vogel, J. Fan, E. Seiler, R. Ries, and X. Jiang, Superconducting nbn thin films for use in superconducting radio frequency cavities, *Supercond. Sci. Technol.* **34**, 025006 (2020).
 [4] R. Russo, E. Esposito, A. Crescitelli, E. Di Gennaro, A. Vettoliere, R. Cristiano, and M. Lisitskiy, Nanosquids based

on niobium nitride films, *Supercond. Sci. Technol.* **30**, 024009 (2017).
 [5] J. J. Renema, R. Gaudio, Q. Wang, Z. Zhou, A. Gaggero, F. Mattioli, R. Leoni, D. Sahin, M. J. A. de Dood, A. Fiore, and M. P. van Exter, Experimental test of theories of the detection mechanism in a nanowire superconducting single photon detector, *Phys. Rev. Lett.* **112**, 117604 (2014).
 [6] Y. Ikebe, R. Shimano, M. Ikeda, T. Fukumura, and M. Kawasaki, Vortex dynamics in a NbN film studied by terahertz spectroscopy, *Phys. Rev. B* **79**, 174525 (2009).
 [7] P. Lipavský, A. Elmurodov, P.-J. Lin, P. Matlock, and G. R. Berdiyrov, Effect of normal current corrections on the vortex

- dynamics in type-II superconductors, *Phys. Rev. B* **86**, 144516 (2012).
- [8] C. Kittel, *Introduction to Solid State Physics*, 8th ed. (John Wiley & Sons, New York, NY, 2004).
- [9] A. T. Dorsey, Vortex motion and the Hall effect in type-II superconductors: A time-dependent Ginzburg-Landau theory approach, *Phys. Rev. B* **46**, 8376 (1992).
- [10] S. Eley, A. Glatz, and R. Willa, Challenges and transformative opportunities in superconductor vortex physics, *J. Appl. Phys.* **130**, 050901 (2021), .
- [11] S. Vegesna, H. Schmidt, D. Buerger, S. Lanka, and S. Linzen, Analysis of low-temperature magnetotransport properties of *NbN* thin films grown by atomic layer deposition, *Magnetochemistry* **8**, 33 (2022).
- [12] S. Linzen, M. Ziegler, O. V. Astafiev, M. Schmelz, U. Hübner, M. Diegel, E. Il'ichev, and H.-G. Meyer, Structural and electrical properties of ultrathin niobium nitride films grown by atomic layer deposition, *Supercond. Sci. Technol.* **30**, 035010 (2017).
- [13] M. Ziegler, S. Linzen, S. Goerke, U. D.-I. Brückner, J. Plentz, J. Dellith, A. Himmerlich, M. Himmerlich, U. Hübner, S. Krischok, and H.-G. Meyer, Effects of plasma parameter on morphological and electrical properties of superconducting NbN deposited by MO-PEALD, *IEEE Trans. Appl. Supercond.* **27**, 1 (2017).
- [14] E. Knehr, M. Ziegler, S. Linzen, K. Ilin, P. Schanz, J. Plentz, M. Diegel, H. Schmidt, E. Il'ichev, and M. Siegel, Wafer-level uniformity of atomic-layer-deposited niobium nitride thin films for quantum devices, *J. Vac. Sci. Technol.* **39**, 052401 (2021).
- [15] B. T. Matthias, T. H. Geballe, and V. B. Compton, Errata: Superconductivity, *Rev. Mod. Phys.* **35**, 414(E) (1963).
- [16] M. Tinkham, *Introduction to Superconductivity*, 2nd ed. (McGraw-Hill, New York, NY, 1996).
- [17] X. Wei, P. Roy, Z. Yang, D. Zhang, Z. He, P. lu, O. Licata, H. Wang, B. Mazumder, N. Patibandla, Y. Cao, H. Zeng, M. Zhu, and Q. Jia, Ultrathin epitaxial nbn superconducting films with high upper critical field grown at low temperature, *Mater. Res. Lett.* **9**, 336 (2021).
- [18] M. Belogolovskii, M. Poláčková, E. Zhitlukhina, B. Grančič, L. Satrapinskyy, M. Gregor, and T. Plecenik, Competing length scales and 2D versus 3D dimensionality in relatively thick superconducting nbn films, *Sci. Rep.* **13**, 19450 (2023).
- [19] J. Sonier, Investigations of the core structure of magnetic vortices in type-II superconductors using muon spin rotation, *J. Phys.: Condens. Matter* **16**, S4499 (2004).
- [20] F. Gunkel, C. Bell, H. Inoue, B. Kim, A. G. Swartz, T. A. Merz, Y. Hikita, S. Harashima, H. K. Sato, M. Minohara, S. Hoffmann-Eifert, R. Dittmann, and H. Y. Hwang, Defect control of conventional and anomalous electron transport at complex oxide interfaces, *Phys. Rev. X* **6**, 031035 (2016).
- [21] P. Mandal, S. K. Ojha, R. K. Patel, S. Kumar, and S. Middey, Observation of the anomalous Hall effect in NdTiO₃/SrTiO₃ heterostructures, *J. Phys. Chem. C* **125**, 12968 (2021).
- [22] O. Lindberg, Hall effect, *Proc. IRE* **40**, 1414 (1952).
- [23] O. Riss, E. Shaked, M. G. Karpovsky, and A. Gerber, Offset reduction in Hall effect measurements using a nonswitching van der pauw technique, *Rev. Sci. Instrum.* **79**, 073901 (2008).
- [24] W.-K. Kwok, U. Welp, A. Glatz, A. E. Koshelev, K. J. Kihlstrom, and G. W. Crabtree, Vortices in high-performance high-temperature superconductors, *Rep. Prog. Phys.* **79**, 116501 (2016).
- [25] K. Harada, T. Matsuda, J. E. Bonevich, M. Igarashi, S. Kondo, G. Pozzi, U. Kawabe, and A. Tonomura, Real-time observation of vortex lattices in a superconductor by electron microscopy, *Nature (London)* **360**, 51 (1992).
- [26] I. Esmail Zadeh, J. Chang, J. Los, S. Gyger, A. W. Elshaari, S. Steinhauer, S. Dorenbos, and V. Zwiller, Superconducting nanowire single-photon detectors: A perspective on evolution, state-of-the-art, future developments, and applications, *Appl. Phys. Lett.* **118**, 190502 (2021).
- [27] G. Gol'tsman, O. Okunev, G. Chulkova, A. Lipatov, A. Semenov, K. Smirnov, B. Voronov, A. Dzardanov, G. Williams, and R. Sobolewski, Picosecond superconducting single photon optical detector, *Appl. Phys. Lett.* **79**, 705 (2001).
- [28] A. Semenov, P. Haas, H.-W. Hübers, K. Ilin, M. Siegel, A. Kirste, D. Drung, T. Schurig, and A. Engel, Intrinsic quantum efficiency and electro-thermal model of a superconducting nanowire single-photon detector, *J. Mod. Opt.* **56**, 345 (2009).
- [29] K. L. Nicolich, C. Cahall, N. T. Islam, G. P. Lafyatis, J. Kim, A. J. Miller, and D. J. Gauthier, Universal model for the turn-on dynamics of superconducting nanowire single-photon detectors, *Phys. Rev. Appl.* **12**, 034020 (2019).
- [30] A. Engel, J. Renema, K. Ilin, and A. Semenov, Detection mechanism of superconducting nanowire single-photon detectors, *Supercond. Sci. Technol.* **28**, 114003 (2015).
- [31] L. N. Bulaevskii, M. J. Graf, and V. G. Kogan, Vortex-assisted photon counts and their magnetic field dependence in single-photon superconducting detectors, *Phys. Rev. B* **85**, 014505 (2012).
- [32] I. Charaev, A. Semenov, K. Ilin, and M. Siegel, Magnetic-field enhancement of performance of superconducting nanowire single-photon detector, *IEEE Trans. Appl. Supercond.* **29**, 2200605 (2019).
- [33] G. Blatter, M. V. Feigel'man, V. B. Geshkenbein, A. I. Larkin, and V. M. Vinokur, Vortices in high-temperature superconductors, *Rev. Mod. Phys.* **66**, 1125 (1994).
- [34] S. L. Sondhi, S. M. Girvin, J. P. Carini, and D. Shahar, Continuous quantum phase transitions, *Rev. Mod. Phys.* **69**, 315 (1997).
- [35] S. Sachdev, *Quantum Phase Transitions* (Cambridge University Press, Cambridge, UK, 1999).
- [36] S. J. Hagen, C. J. Lobb, R. L. Greene, M. G. Forrester, and J. H. Kang, Hall effect in the mixed state of high-T_c superconductors, *Phys. Rev. B* **41**, 11630 (1990).